The Meteoritical Society

Meteoritics & Planetary Science 48, Nr 12, 2577–2596 (2013)
doi: 10.1111/maps.12238

Cathodoluminescence microscopy and spectroscopy of forsterite from Kaba meteorite: An application to the study of hydrothermal alteration of parent body

Arnold GUCSIK[1,2*], Taro ENDO[3], Hirotsugu NISHIDO[3], Kiyotaka NINAGAWA[4], Masahiro KAYAMA[5], Szaniszló BÉRCZI[6], Szabolcs NAGY[7], Péter ÁBRAHÁM[2], Yuki KIMURA[8], Hitoshi MIURA[8], Ildikó GYOLLAI[9], Irakli SIMONIA[10], Péter RÓZSA[11], József POSTA[11], Dániel APAI[12], Krisztián MIHÁLYI[11], Mihály NAGY[13], and Ulrich OTT[14]

[1]Department of Geology, University of Johannesburg, 2600 Auckland Park, Johannesburg, South Africa
[2]Konkoly Thege Miklos Astronomical Institute, Research Centre for Astronomy and Earth Sciences, Konkoly Thege Miklós út 15-17, Budapest H-1121, Hungary
[3]Department of Biosphere-Geosphere System Science, Okayama University of Science, 1-1 Ridai-cho, Okayama 700-0005, Japan
[4]Department of Applied Physics, Okayama University of Science, 1-1 Ridai-cho, Okayama 700-0005, Japan
[5]Department of Earth and Planetary Systems Science, Graduate School of Science, Hiroshima University, Kagami-yama 1-3-1, Higashi-Hiroshima, Hiroshima 739-8526, Japan
[6]Institute of Physics, Department of Material Physics, Eötvös University, Pázmány P. s. 1/a, Budapest H-1117, Hungary
[7]Department of Mineralogy, Petrology and Geochemistry, University of Szeged, Egyetem utca 2, Szeged H-6722, Hungary
[8]Department of Earth and Planetary Materials Science, Graduate School of Science, Tohoku University, Sendai 980-8578, Japan
[9]Department of Lithospheric Research, Center for Earth Sciences, University of Vienna, Althanstrasse 14, Vienna A-1090, Austria
[10]School of Graduate Studies of Ilia State University, Tbilisi, Georgia
[11]University of Debrecen, Egyetem tér 1, Debrecen H-4032, Hungary
[12]Lunar and Planetary Laboratory, Department of Planetary Sciences, The Arizona University, 1629 E. University Blvd, Tucson, Arizona 85721–0092, USA
[13]Reformed College of Debrecen, Kálvin tér 16., Debrecen H-4026, Hungary
[14]Savaria University Center, University of West Hungary, Károlyi Gáspár tér 4, Szombathely H-9700, Hungary
[*]Corresponding author. E-mail: argu1986@hotmail.com

(Received 13 April 2011; revision accepted 23 October 2013)

Abstract–Highly forsteritic olivine (Fo: 99.2–99.7) in the Kaba meteorite emits bright cathodoluminescence (CL). CL spectra of red luminescent forsterite grains have two broad emission bands at approximately 630 nm (impurity center of divalent Mn ions) in the red region and above 700 nm (trivalent Cr ions) in the red–IR region. The cores of the grains show CL blue luminescence giving a characteristic broad band emission at 400 nm, also associated with minor red emissions related to Mn and Cr ions. CL color variation of Kaba forsterite is attributed to structural defects. Electron probe microanalyzer (EPMA) analysis shows concentrations of Ca, Al, and Ti in the center of the forsterite grain. The migration of diffusible ions of Mn, Cr, and Fe to the rim of the Kaba meteoritic forsterite was controlled by the hydrothermal alteration at relatively low temperature (estimated at about 250 °C), while Ca and Al ions might still lie in the core. A very unusual phase of FeO (wüstite) was also observed, which may be a terrestrial alteration product of FeNi-metal.

INTRODUCTION

Kornacki and Wood (1984) were the first investigators to study samples from the Kaba meteorite on the subject of the matrix olivine. Hua and Buseck (1995, 1998) identified fayalite, and later fayalitic halos, in forsterite. Choi et al. (2000) suggested that the fayalite in the Kaba meteorite might have formed by replacement of pre-existing magnetite and silica, based on the O-isotopic compositions of magnetite and olivine. Valera et al. (2000) detected variation in carbon content of glass inclusions in olivines ranging from 250

to 2090 μg g^{-1}. According to Hua et al. (2005), Cr isotopes in fayalite indicate that this mineral formed about 9.7 Ma after the formation of calcium-aluminum-rich inclusions (CAIs). More recently, micro-Raman spectroscopy of forsterite indicated the highly crystalline nature of the Kaba forsterite (Gucsik et al. 2011).

Kaba (CV3) is one of the most primitive carbonaceous chondrites (e.g., Krot et al. 1998; Bonal et al. 2006). This meteorite is, therefore, of great interest to us because it will give us a better understanding of the mineralogy of CV3s. Cathodoluminescence (CL) has been used to characterize meteoritic minerals, especially olivine (forsterite), for the investigation of their thermal history, due to high detection sensitivities for structural defects and activator elements, with high spatial resolution.

The purpose of this paper is to describe detailed observations of CL emissions from olivine and other phases from the Kaba chondrite and to clarify the relationship between the CL spectra and the defects in crystals. Furthermore, it is also an aim of this contribution to discuss the CL properties of forsterite and the implication for dust evolution in the early solar system. The spectroscopic information on CL is especially important because it can be attributed to specific defects and/or impurities (e.g., Gucsik et al. 2012; Nishido et al. [2013] and references therein), which should thus be key to understanding the formation environment of the minerals, including the process of the hydrothermal alteration in the parent body.

SAMPLE AND EXPERIMENTAL PROCEDURES

The Kaba meteorite sample kept at the University of Debrecen was employed for petrographic observations under a polarizing light microscope, CL measurements, and electron microprobe analyses (EPMA).

Following a systematic optical microscope-cathodoluminescence study of a Kaba thin section, seven representative grains (designated as B-1 through B-7) were selected for further analyses because they did not contain any irregular fracturing or crystallographic imperfections (Fig. 1).

Semiquantitative analyses for major elements of constituent minerals in the Kaba meteorite were conducted by energy-dispersive spectrometry (EDS) with an ISIS analysis system (Oxford) linked to a JEOL JSM-5410LV scanning electron microscope (SEM). The accelerating voltage was 15 kV and the beam current was 2.0 nA, with a focused beam. Also, the SEM and backscattered electron (BSE) images were captured by JSM-5410LV SEM.

Quantitative analyses for minor and major elements in olivine were obtained by wavelength-dispersive

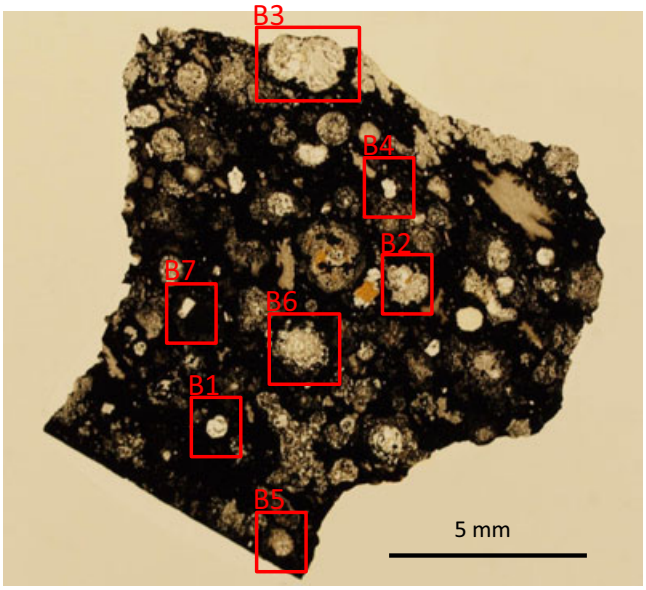

Fig. 1. Plane-polarized image of the Kaba meteorite sample showing the analyzed areas of this study.

spectrometry (WDS) linked to a JEOL JXA-8900R SEM. Operational conditions for the standard analysis and quantitative analysis of unknown minerals were an accelerating voltage of 15 kV and a probe current of 40 nA on a Faraday cup equipped with PCD (probe current detector), using a focused beam. The ZAF program installed in the workstation was employed for matrix corrections. Seven standard minerals were selected as follows: periclase, corundum, wollastonite, rutile, eskolaite, manganosite, and hematite. Among the detected elements were Mg, Al, Ca, Si, Ti, Cr, Mn, and Fe, for which X-ray distribution maps were made by the WDS operated with an accelerating voltage of 15 kV and beam current 100 nA, with a focused beam.

The detection limit for quantitative analysis (WDS) ranged between 0.03 (light elements) and 0.04 (heavy elements) wt%, and was around 0.005 wt% for the qualitative measurements by EDS.

Cathodoluminescence color imaging was carried out using a luminoscope (ELM-3R) consisting of a cooled charge-coupled device (CCD) camera, a cold cathode discharge tube, and a vacuum chamber. This was operated with electron beams generated by excitation voltage at 10 kV and beam current of 0.5 mA at vacuum condition, i.e., less than 100 Torr. A magnet was used to control the diameter of electron beam spot at a few millimeter sizes on the sample surface. CL images were converted to digital data using the Nikon imaging system (DS-5Mc).

A Mini-CL detector (Gatan) consisting of a multialkali photomultiplier tube installed in the

JSM-5410LV SEM was used to obtain the CL scanning images at high magnification. A scanning electron microscope–cathodoluminescence (SEM–CL) system containing a SEM (JEOL: JSM-5410LV) combined with a grating monochromator (OXFORD: Mono CL2), having a retractable parabolic mirror coated with aluminum (collecting efficiency of 75%), provided the CL spectral measurements for this study. The CL was dispersed by a grating monochromator with the following characteristics: 1200 grooves mm^{-1}, a focal length of 0.3 m, F of 4.2, limit of resolution of 0.5 nm, and slit width of 4 mm at the inlet and outlet. CL spectral data were recorded by a photon counting method using a photomultiplier tube (Hamamatsu: R2228) and converted to digital data.

Further details of the CL equipment and analytical procedure can be found in Kayama et al. (2010). Corrected CL spectra in energy units were deconvoluted into the Gaussian components corresponding to each emission center. A peak-fitting software (Peak Analyzer) in OriginPro 8J SR2 was used for the correction and deconvolution of each emission center.

RESULTS

Petrographical Description of the Mineral Constituents in the Kaba Meteorite

The Kaba meteorite has a chondritic texture containing characteristic chondrules, CAIs, amoeboid olivine aggregates (AOA), and several other fragments embedded in very fine-grained matrix. Modal abundances in Kaba revealed by point counting are matrix (55.2%), chondrule (27.7%), CAIs (3.4%), AOAs (2.5%), isolated coarse-grained olivine (0.8%), and unclassified (10.4%). Compared to Hezel et al. (2008) and Hezel and Kießwetter (2010), Our modal abundance is not in agreement with the literature of Hezel et al. (2008) and Hezel and Kießwetter (2010). Several types of chondrules occur in the Kaba meteorite that are associated with porphyritic, granular, radial, and barred olivine. Diameters of the chondrules are between 70 μm and 1.4 mm. The maximum size of AOAs is 0.5 × 1.7 mm with an irregular shape. Coarse-grained olivine (isolated olivine, embedded in matrix) exhibits a round shape with a maximum diameter of 0.5 mm.

Porphyritic forsterite grains, a spherical Fe-rich phase, and mesostasis are associated with porphyritic olivine chondrules, which occur with a diameter of approximately 1.2 mm on average (Fig. 2A). The forsterite composition is $Fo_{99.7}$, as summarized in Table 1. The mesostasis consists mostly of feldspar with $An_{78}Ab_{22}$ composition. Pentlandite and a very rare phase of FeO (wüstite-alteration product of FeNi metal) occur in the Fe-rich phase.

The diameters of the granular olivine-pyroxene chondrules are about 0.5 × 0.3 mm in average size (Fig. 2B). They have an elliptic shape and consist of porphyritic olivine grains with Fo_{99} composition, intergranular grains of diopside with $En_{56.6}Wo_{42.2}$ composition, and an Fe-rich phase (Table 1).

Coarse grains of olivine (up to 150 μm) and fractured small grains of olivine are dominant in the AOAs (Figs. 2C and 2D). The olivine grains have a variable composition, including forsterite ($Fo_{97.2–99.6}$) and fayalite ($Fa_{81.7}$) (Table 1). Coarse-grained olivine includes internally distributed micrometer-sized diopside with $Wo_{55.8}En_{43.6}Fs_{0.6}$ and anorthite with $An_{96.1}Ab_{3.9}$ (Table 1).

Isolated olivine grains (sizes: 100–250 μm) occur in the matrix and consist of forsterite with $Fo_{99.2–99.8}$ composition (Fig. 2E), which are associated with complex aggregates of porphyritic olivine and enstatite (Fig. 2F; Table 1). Forsterite near endmember composition coexists with enstatite, while fayalite near-endmember composition is scattered together with magnetite and troilite.

Luminescence Microscopy

Six olivine grains (named B-1 to B-6) including typical characteristic luminescent forsterite and mesostasis in chondrules were selected for detailed analyses by CL microscopy and spectrometry using a SEM–CL system attached to EPMA. Figure 1 shows the selected grains indicated as quadrangle frames and their color CL images were compiled in Fig. 3. CL imaging exhibits characteristic features of the emissions of bright red color in AOA, within chondrules and isolated olivine grains in matrix. CAIs scattered in mesostasis and matrix exhibit a blue to violet luminescence. The mesostasis in chondrules is characterized by yellow to green luminescence. The following section is based on a description of chemical profiling and X-ray mapping for grains B-1, B-2, B-4, and B-5 by EPMA analysis using WDS.

Scanning Electron Microscope-Cathodoluminescence Study of Kaba Olivine Grains and Mesostasis

Rounded Olivine Grain (B-1 Area)

Figure 4A consists of two olivine crystals. A relatively big as well as rounded olivine grain (approximately 400 μm in diameter) embedded in matrix exhibits clear and unaltered features, but with irregular cracks, under a polarizing microscope (Fig. 4A). The BSE image shows a homogeneous mineral phase (Fig. 5A), but inhomogeneous

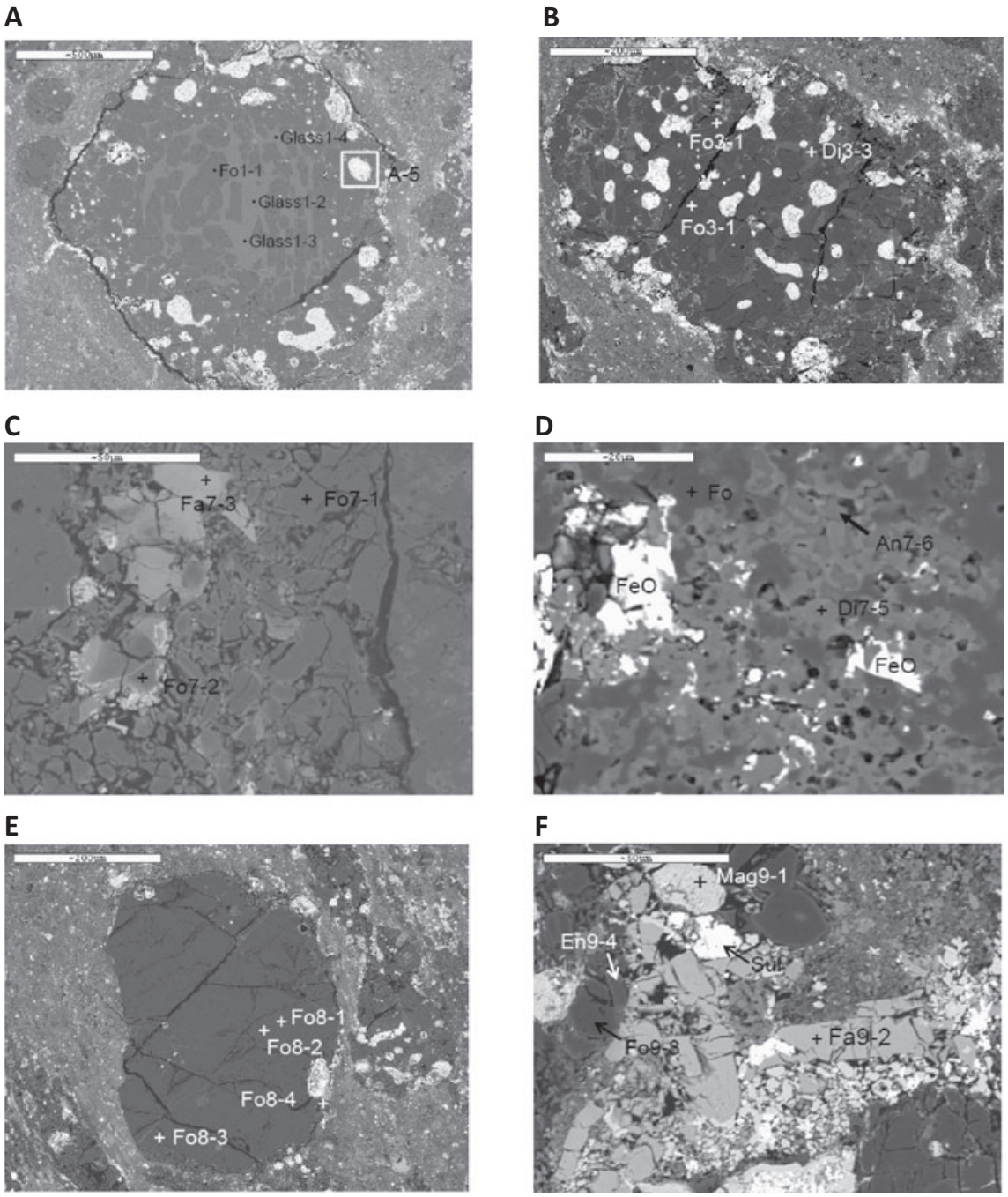

Fig. 2. Scanning electron microscope images of A) porphyritic olivine chondrule, B) granular olivine-pyroxene, C) amoeboid olivine aggregates, D) with its anorthite phase, E) an isolated olivine grain, and F) complex aggregates representing the analyzing points for the EMP analyses as shown in Table 1.

distribution of CL emission, which can be recognized in the CL image (Fig. 4B), where intensity decreases toward the outer edge of the grain. The CL spectra contain three luminescent components at about 400, 640, and above 700 nm, which were obtained from four areas, including two core and two rim parts in the grain (Fig. 4C). The core of the olivine grain shows a brighter CL emission in blue and red–IR regions than the rim, whereas the rim of the olivine grain shows a brighter CL emission at 640 nm in the red region than the core.

Elemental zoning profiles along the AB-trace (Fig. 5A) are shown for CaO, Al_2O_3, and TiO_2 (Fig. 5B) and for FeO, MnO, NiO, and Cr_2O_3 (Fig. 5C). Concentrations of Ca and Al increase toward

Table 1. Chemical composition of the Kaba forsterite obtained by EMP analysis.

Occurence	Sample	SiO_2	TiO_2	Al_2O_3	FeO	Cr_2O_3	MnO	MgO	CaO	NiO	Na_2O	Total (wt%)	Fo	Fs	En	Wo
Porphyritic chondrule																
Forsterite	Fo1-1	43.14	<0.04	0.23	0.30	0.33	<0.04	55.00	0.34	<0.04	0.53	99.87	99.7			
Glass	Glass1-2	52.52	0.85	22.13	<0.04	0.46	<0.04	5.52	15.68	<0.04	2.35	99.51				
Glass	Glass1-3	52.32	0.84	22.13	0.48	0.46	<0.04	5.41	16.76	<0.04	1.58	99.98				
Glass	Glass1-4	52.74	0.89	22.58	<0.04	0.27	<0.04	4.68	16.99	<0.04	1.63	99.78				
FeO	FeO1-5	<0.04	<0.04	<0.04	97.63	0.51	<0.04	0.28	<0.04	<0.04	0.52	98.94				
Granular olivine-pyroxene chondrule																
Forsterite	Fo3-1	42.88	<0.04	<0.04	0.89	0.61	<0.04	54.99	0.19	<0.04	0.38	99.94	99.1			
Forsterite	Fo3-2	42.76	<0.04	<0.04	1.02	0.31	<0.04	54.70	0.23	<0.04	0.45	99.47	99.0			
Diopside	Di3-3	51.56	1.08	7.72	0.68	1.04	<0.04	18.23	18.92	<0.04	0.44	99.67		1.2	56.6	42.2
AOA																
Forsterite	Fo7-1	43.35	<0.04	<0.04	0.41	0.22	0.39	55.03	<0.04	<0.04	0.46	99.86	99.6			
Forsterite	Fo7-2	43.07	<0.04	0.22	2.71	0.52	0.57	52.58	<0.04	<0.04	0.42		97.2			
Forsterite	Fo7-3	31.90	<0.04	<0.04	59.01	<0.04	0.93	7.40	<0.04	<0.04	0.48	99.72	18.3			
Diopside	Di7-5	50.41	0.62	8.73	0.33	<0.04	<0.04	14.25	25.36	<0.04	0.40			0.6	43.6	55.8
Anorthite	An7-6	43.33	0.38	33.85	<0.04	<0.04	<0.04	1.15	20.39	<0.04	0.58	99.68				
Isolated olivine grain																
Forsterite	Fo8-1	42.07	0.07	0.29	0.21	0.05	<0.04	56.65	0.88	<0.04	<0.04		99.8			
Forsterite	Fo8-2	42.91	0.04	0.27	0.21	0.06	<0.04	56.91	0.85	<0.04	<0.04		99.8			
Forsterite	Fo8-3	42.26	<0.04	<0.04	0.52	0.18	<0.04	55.10	0.37	<0.04	<0.04	98.47	99.5			
Forsterite	Fo8-4	42.16	<0.04	0.04	0.86	0.34	0.06	57.30	0.25	<0.04	<0.04		99.2			
Complicated aggregates																
Magnetite	Mag9-1	2.41	<0.04	<0.04	90.29	2.72	<0.04	0.90	0.54	0.75	0.70	98.31				
Fayalite	Fa9-2	29.90	<0.04	<0.04	68.05	<0.04	0.65	0.26	<0.04	<0.04	0.50	99.36	0.7			
Forsterite	Fo9-3	43.19	<0.04	<0.04	0.60	0.36	<0.04	54.95	0.22	<0.04	0.41	99.73	99.4			
Enstatite	En9-4	58.93	0.46	1.57	1.21	<0.04	<0.04	36.30	0.52	<0.04	0.59	99.58		1.8	97.2	1.0

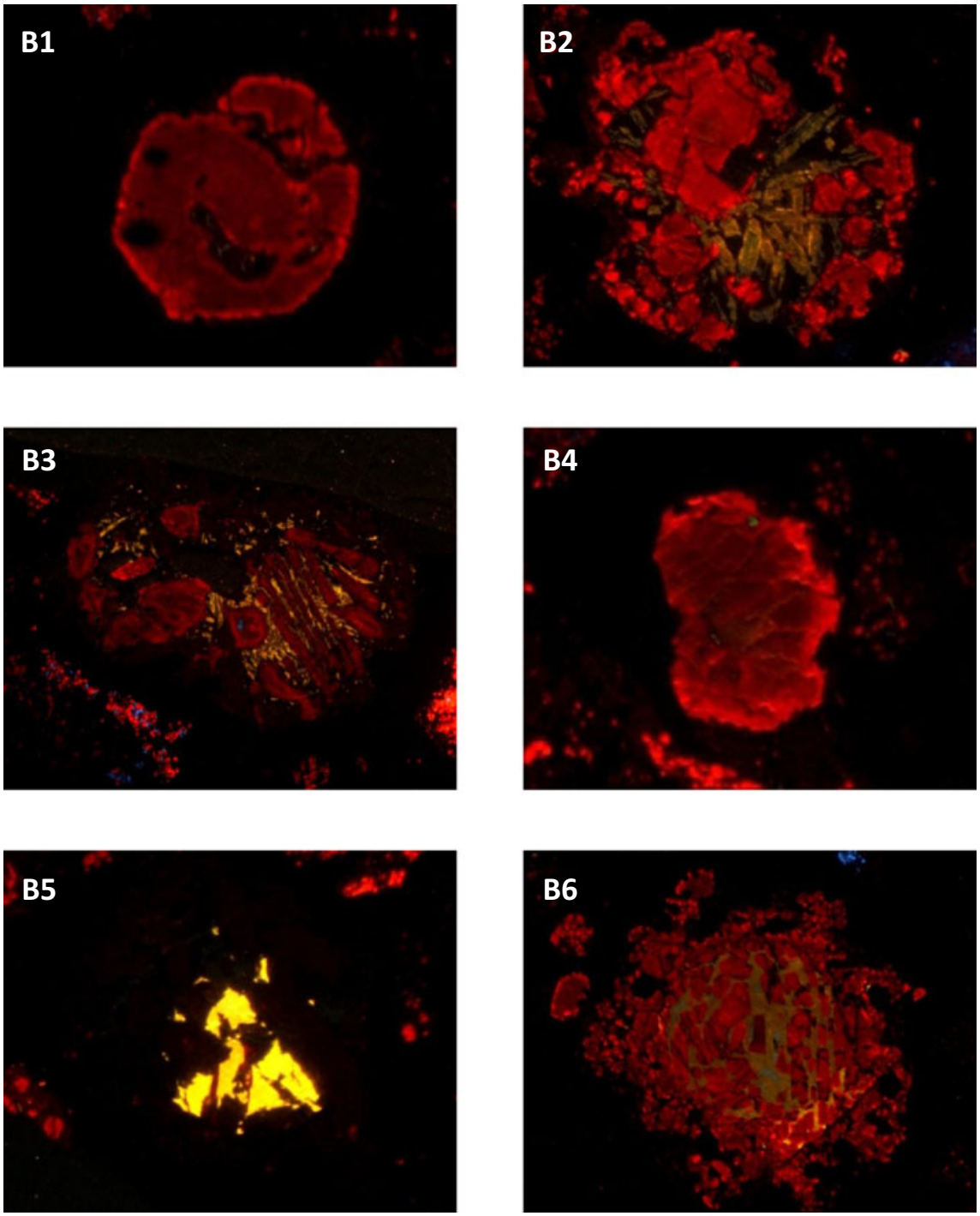

Fig. 3. Color cathodoluminescence images of Kaba meteorite (associated with the analyzed areas in Fig. 1) were obtained over the sample by using a luminoscope. Scale bar corresponds to 0.2 mm.

the center of the grain. The concentration of Ti has a similar trend as the variations of Ca and Al, but has a small range. CaO and Al_2O_3 concentrations are approximately 0.6 and 0.25 wt% in the core, and those of the rim are 0.3 and 0.1 wt%, respectively. FeO, MnO, and Cr_2O_3 concentrations are constant with low level in the core, and increase in the rim. We assume that Cr occurs as chromite inclusions in the rims. This chromite may be the result of low-T alteration under oxidizing conditions with Cr^{2+} present in the olivine cores. Fe and Mn diffused inward during the same process mentioned above.

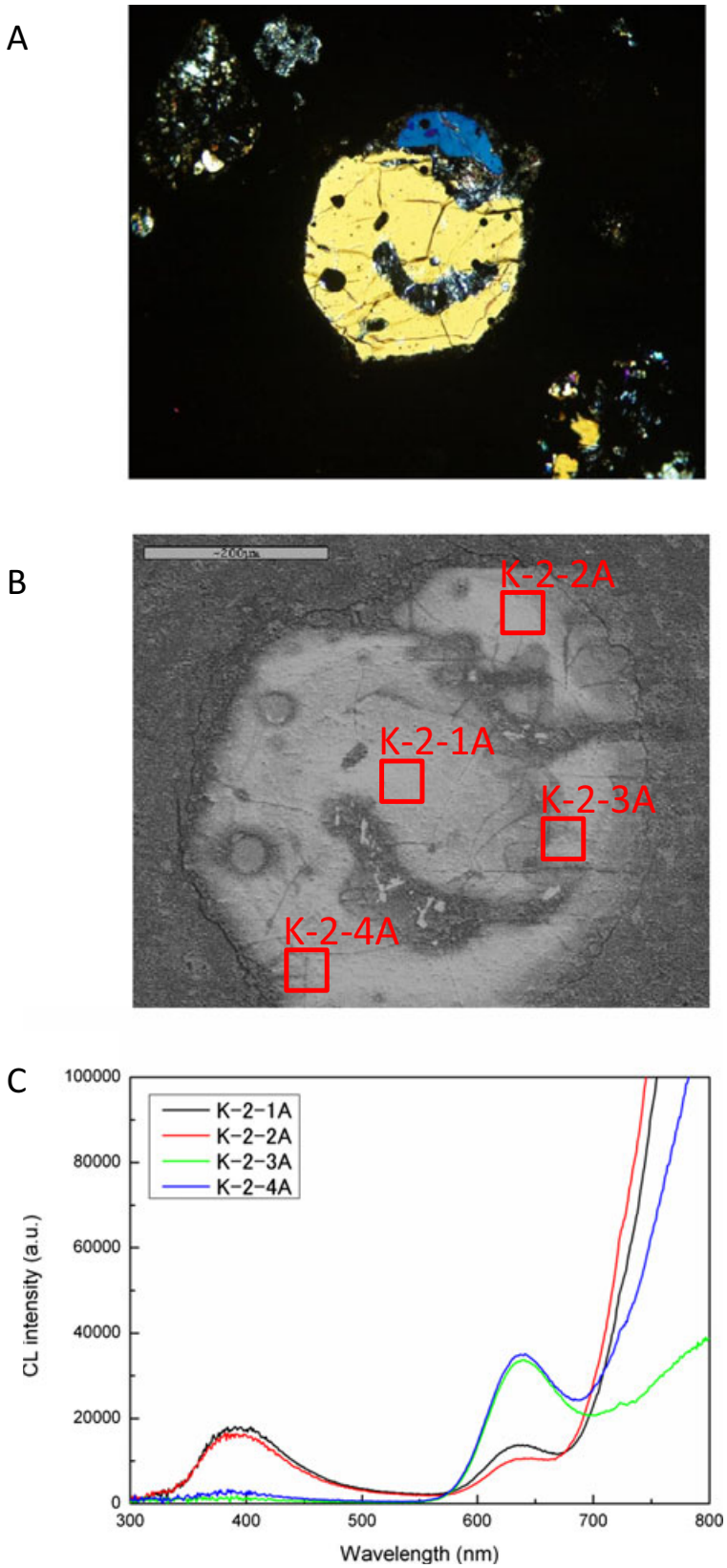

Fig. 4. A) Cross-polarized optical microscope and B) scanning electron microscope-cathodoluminescence (SEM–CL) images of the rounded olivine grain embedded in matrix (B-1 area) including the analyzing points for the C) CL spectral features.

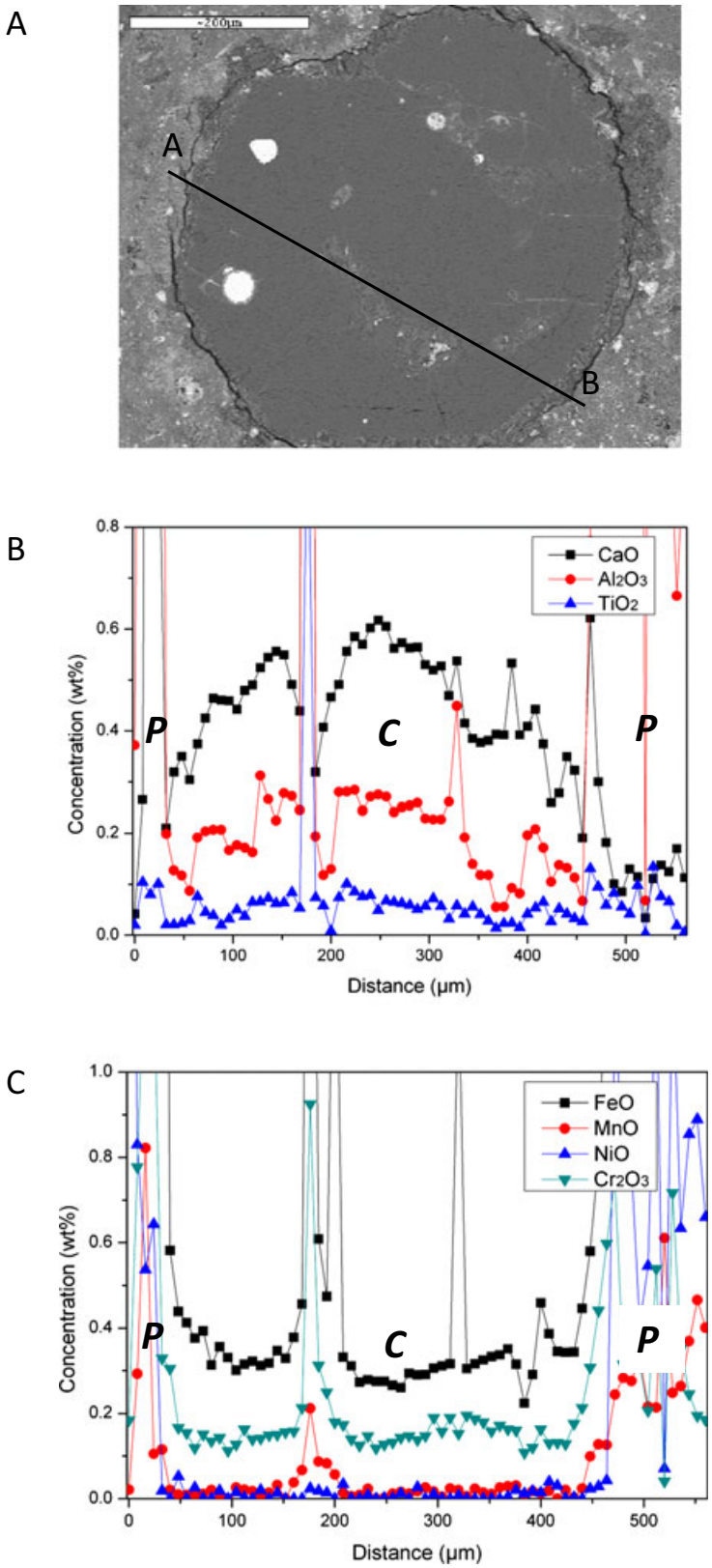

Fig. 5. Backscattered electron image of the A) rounded olivine grain obtained by a scanning electron microscope shows the AB-trace and chemical profiles for B) CaO, Al_2O_3, and TiO_2, and C) for FeO, MnO, NiO, and Cr_2O_3. ***P*** corresponds to the peripheries and ***C*** denotes cores of the selected olivine grain.

Porphyritic Olivine Grains in Chondrule (B-2 Area)

The chondrule in area B-2 includes porphyritic olivine grains with unaltered clear texture under a polarized microscope (Fig. 6A). A CL image of the relatively large grain of olivine shows a significantly enhanced bright domain in the core (Fig. 6B), whereas its BSE image shows a homogeneous feature (Fig. 7A). CL spectral analysis reveals that the domain has more pronounced emissions at 400 nm in the blue region and above 700 nm in the red–IR region than those of the rim (Fig. 6c). CL emission of the rim in the blue region is almost invisible. The peak intensities at 640 nm and above 700 nm increase gradually toward the rim from the grain center.

Figures 7B and 7C exhibit chemical profiles of CaO, Al_2O_3, and TiO_2 along the AB-trace as shown in Fig. 7A, and FeO, MnO, NiO, as well as Cr_2O_3 are presented in Fig. 7c. The olivine grain is more enriched in CaO, Al_2O_3, and TiO_2 around the core than in the outer part of the grain as shown in Fig. 7b. A similar high-Al olivine is described by Pack et al. (2004; their fig. 15). CaO, Al_2O_3, and TiO_2 have concentrations of 0.7, 0.5, and 0.08 wt% in the core and 0.1, approximately 0.04 wt% in the outer part of the grain. An opposite behavior is shown by FeO, Cr_2O_3, and MnO, which increase from the center of the grain toward the rim.

Coarse Olivine Grain Embedded in Matrix (B-4 Area)

The microscope observation of the coarse olivine grain embedded in matrix under polarized light revealed that it has cracks and a slightly altered appearance (Fig. 8A), exhibiting a faint interference color in a finely fissured area at the inner part of the grain. This grain shows similar CL zoning (Fig. 8B) as the olivine grain in B-3 area. Compared with a relatively weaker emission at 640 nm of the rim (Fig. 8c), the core of the grain has a higher emission at 400 nm in the blue region and at above 700 nm in the red–IR region. Its BSE image shows homogeneous features (Fig. 9a).

In comparison to the outer part of the grain, CaO and Al_2O_3 are more abundant in the core (Fig. 9B). Concentration of TiO_2 is difficult to determine due to its relatively small amount (<0.05 wt%); however, it seems to have a similar trend. Around the center, concentrations of CaO and Al_2O_3 reach up to 0.8 and 0.25 wt%, but decrease down to 0.2 and 0.05 wt% toward the rim (Fig. 9B). Concentrations of FeO, MnO, and Cr_2O_3 in the core are approximately 0.2, 0.06, and 0.02 wt% (Fig. 9C). X-ray maps of Mg, Fe, Ca, Mn, Al, Cr, Ni, and Ti indicate lower amounts of Ca and Al in the rim than in the core of the grain.

Mesostasis in Chondrule (B-5 Area)

The mesostasis phase in the chondrule consists of plagioclase ($An_{76}Ab_{24}$) with minute spherical inclusions with wavy extinction under a cross-polarized microscope (Figs. 10A and 10B). These inclusions can be observed as tiny particles with red–green interference color only under a polarizing microscope, but cannot be detected by EPMA or Raman analyses. We suppose that these inclusions exist inside the plagioclase grain, not on the surface. Its BSE and CL images show homogeneous features (Figs. 10C and 10D), and CL spectra show two broad bands at about 400 and 570 nm (Fig. 10E).

Forsterite Clusters and Their Monochromatic CL Images in the Selective Wavelength Mode

The color CL image of the B-7 area in Fig. 1 shows olivine aggregates (Fig. 11A), which contain approximately 100 micrometer sized forsterite clusters with typical sector zoning CL patterns. Monochromatic CL images were obtained at the following wavelength modes: 442 (sector zoning pattern) (Fig. 11B), 631 (Fig. 11D), and 756 nm (Fig. 11C). The latter image exhibits relatively high CL intensity compared with the lower wavelength images.

DISCUSSION

Cathodoluminescence Emission Bands in Kaba Forsterite and Their Peak Assignment

In this study, CL spectra of forsterite in the Kaba meteorite contain three luminescent components: at approximately 400 nm wavelength in the blue region, at 640, and above 700 nm in the red–IR region, where their intensities are distinctly different among analyzed areas even in a single grain.

Blue Emission Center at About 400 nm

Emission bands at around 400 nm were detected in most of the forsterite grains, while their CL intensities vary among zonal sectors observed in CL images. The blue emission centers and their peak intensities are strongly correlated with the concentrations of Al_2O_3, CaO, and TiO_2, indicating that they can be assigned to impurity centers of quadrivalent Ti and/or structural defects. This may be caused by structural distortion or unpaired electrons related to substitution of Si and Mg by Al and Ca, respectively (Steele and Smith 1986; Benstock et al. 1997). According to Pack et al. (2005) and Simon et al. (2008), it is important to consider that refractory forsterite also contains Ti^{3+}. However, the defect center derives from O-Al^{-}-O, which has been found in quartz and feldspar minerals and which acts only as the Löwenstein bridge between two adjacent tetrahedra (Marfunin 1979; Slaby et al. 2008). Therefore, the Al-O center caused by Al^{3+} substitution for

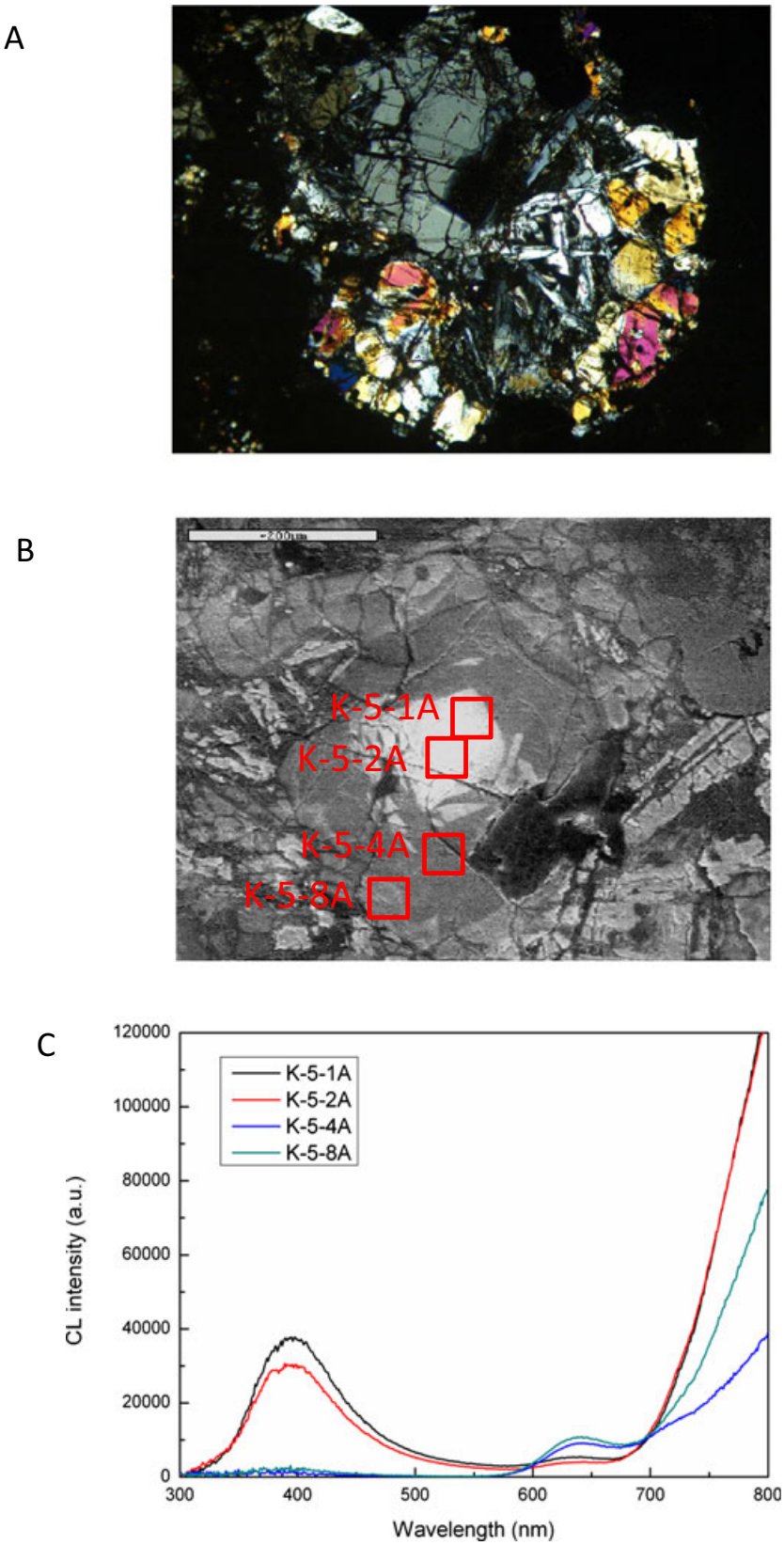

Fig. 6. A) Cross-polarized optical microscope and B) (SEM–CL) images of the porphyritic olivine grains in a chondrule (B-2 area) with C) CL spectra features.

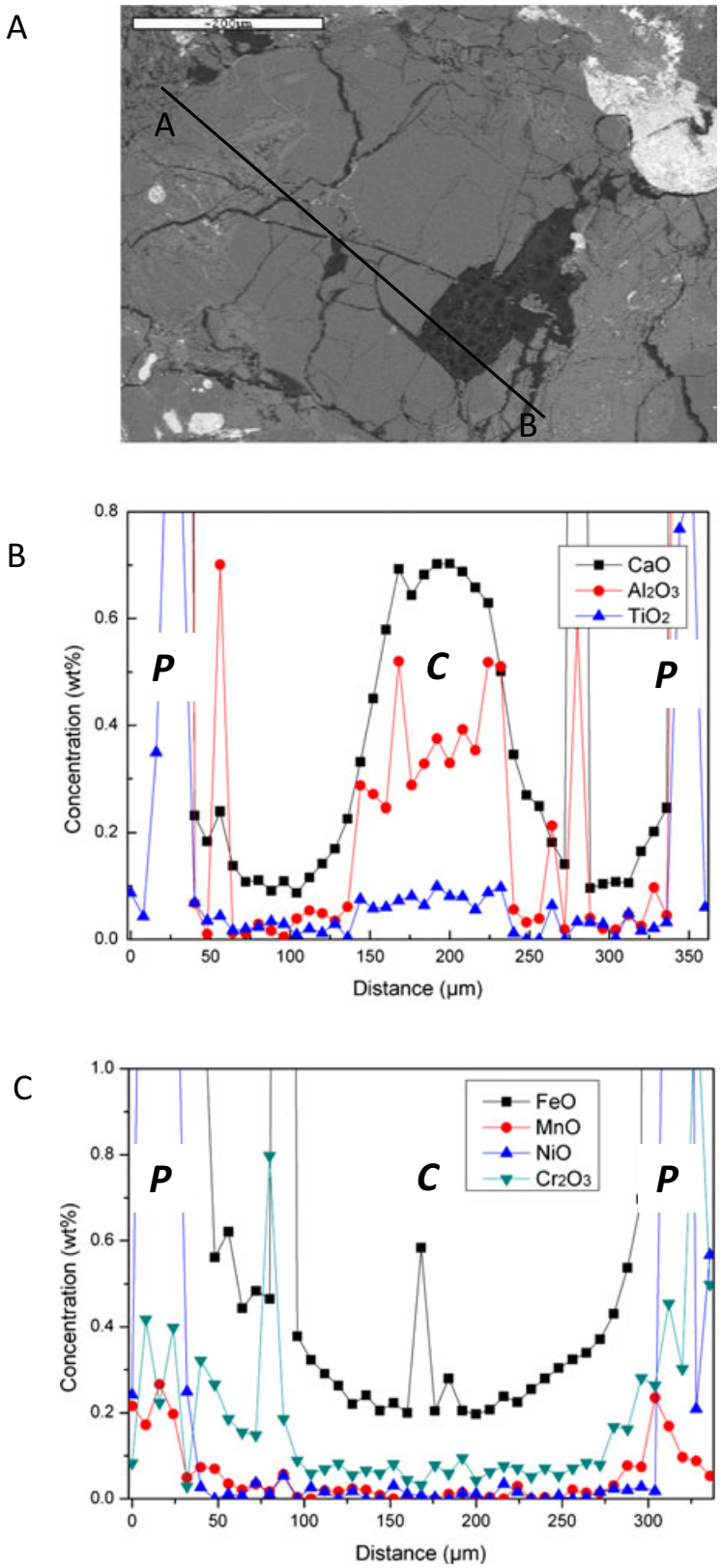

Fig. 7. A) Backscattered electron image exhibits the AB-trace and chemical profiles for B) CaO, Al_2O_3, and TiO_2 and C) for FeO, MnO, NiO, and Cr_2O_3 in the porphyritic olivine grains in a chondrule. ***P*** corresponds to the peripheries and ***C*** denotes cores of the selected olivine grain.

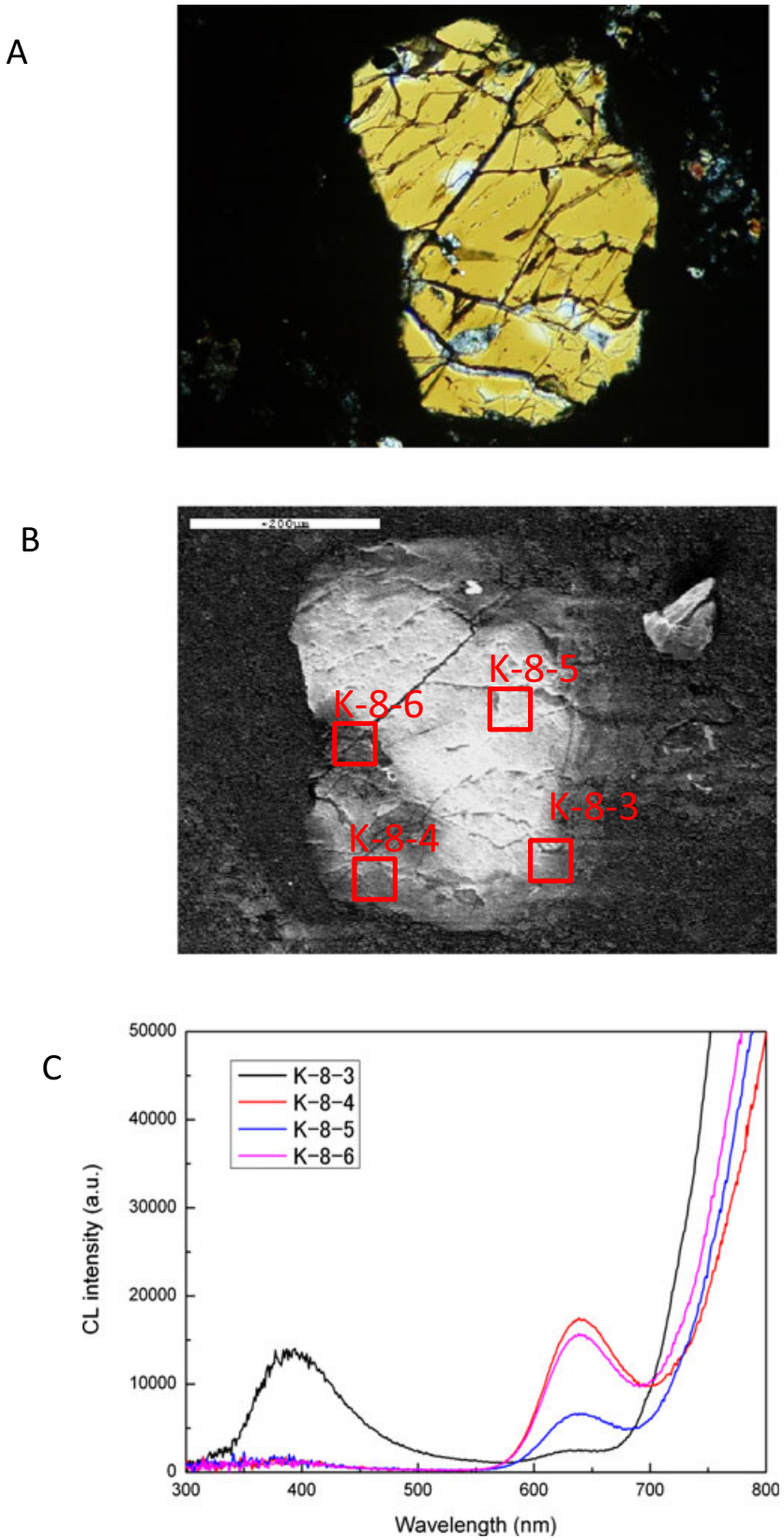

Fig. 8. A) Cross-polarized optical microscope and B) (SEM–CL) B) images of a coarse olivine grain embedded in matrix (B-4 area) with C) CL spectra features.

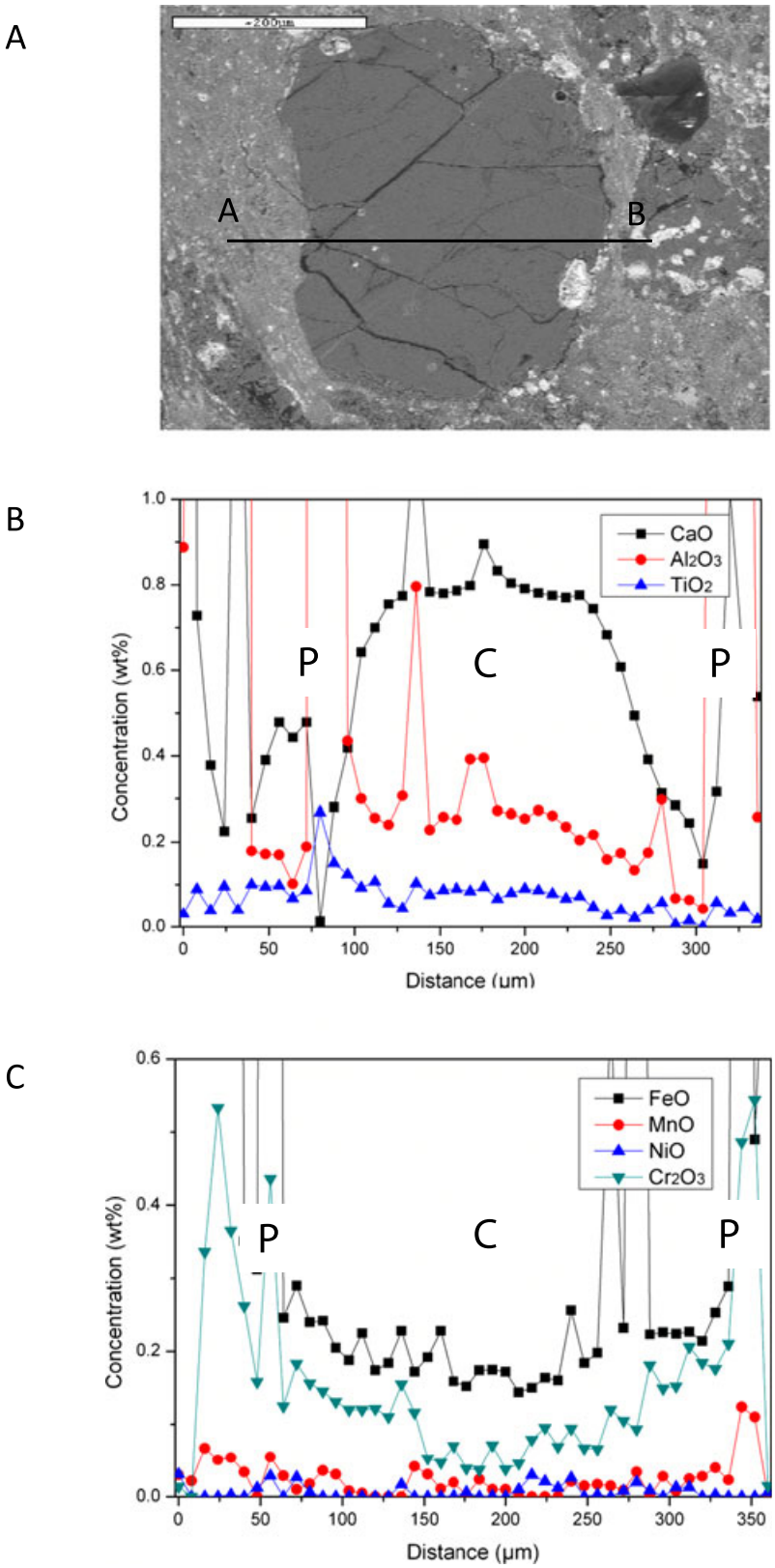

Fig. 9. A) Coarse olivine grain embedded in matrix and its backscattered electron image. The AB-trace and chemical profiles for B) CaO, Al_2O_3, and TiO_2 and C) FeO, MnO, NiO, and Cr_2O_3. ***P*** corresponds to the peripheries and ***C*** denotes cores of the selected olivine grain.

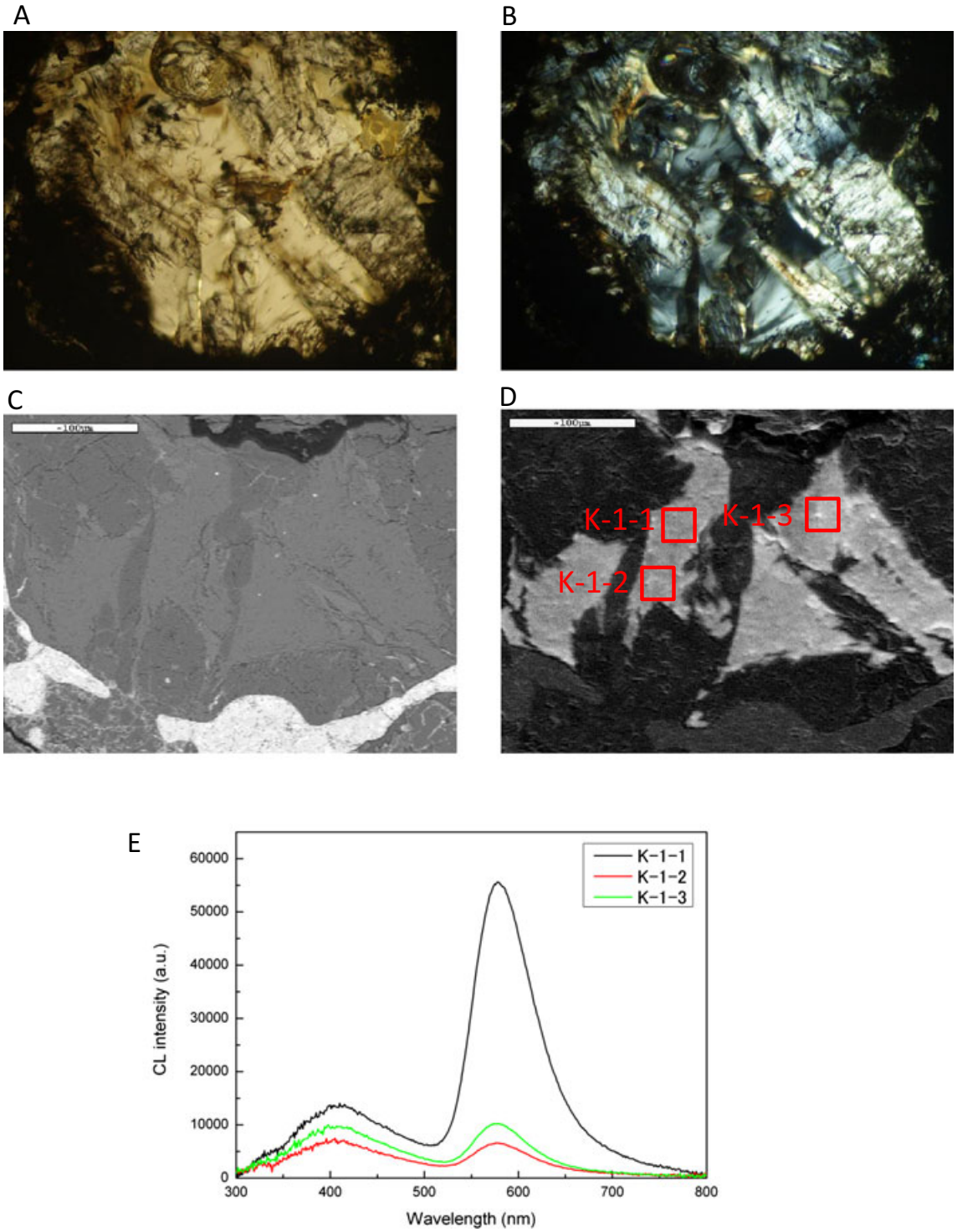

Fig. 10. Optical microscope A) plane polarized, B) cross-polarized, C) BSE, and D) CL images for mesostasis in chondrule (B-5). E) CL spectra of mesostasis in B-5 area.

Si^{4+} (Steele and Smith 1986) is a possible candidate for the origin of broad emission in the blue region, as olivine belongs to a nesosilicate group having isolated tetrahedron with no bridges in the lattice. In most cases, blue CL emission from forsterite is dominated by Ti (possibly present as Ti^{3+} in refractory forsterite) as well as by Al (Pack and Palme 2003). However, Stevens-Kalceff (2009) and Kayama et al. (2010) pointed out that

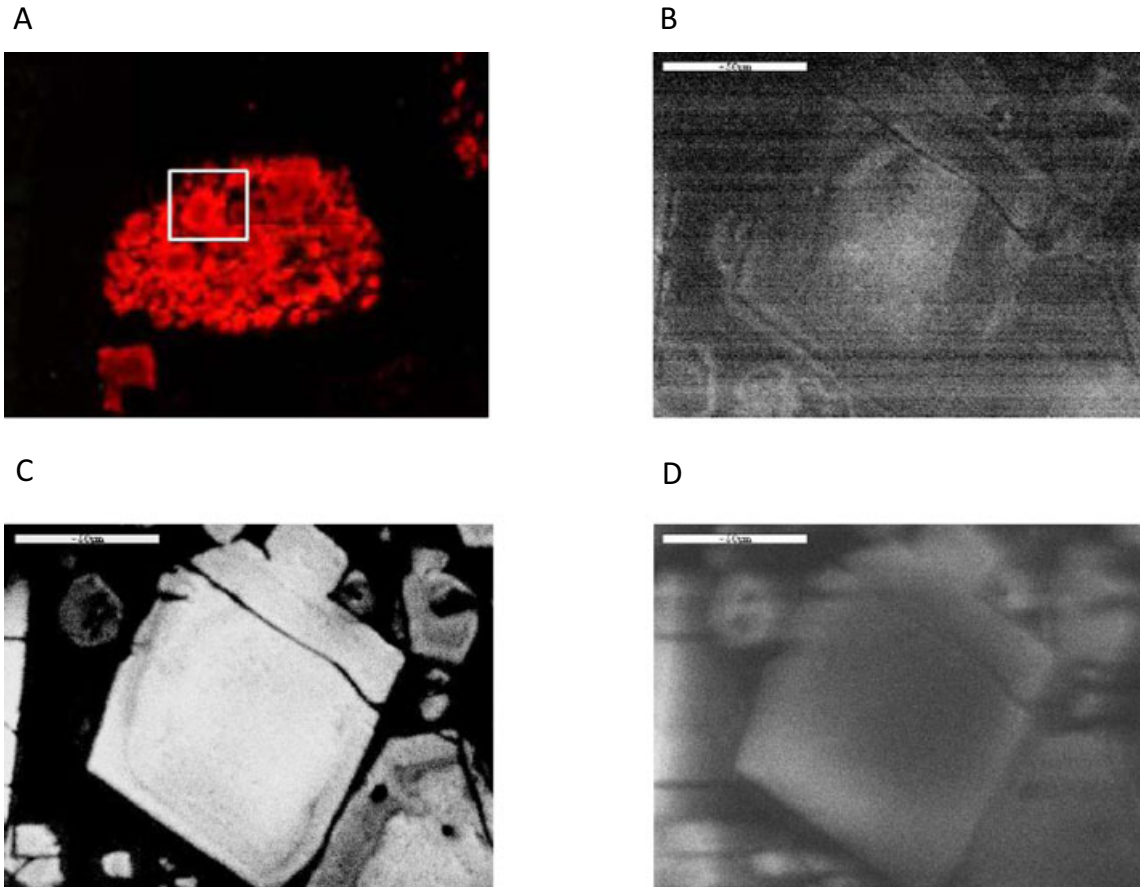

Fig. 11. Color cathodoluminescence (CL) image of the A) olivine cluster in B-7 area and monochromatic CL images obtained at B) 442 nm, C) 756 nm, and D) 631 nm.

the defined component corresponding to the defect center should be verified by further investigations, for example, by electron spin resonance (ESR) measurements.

Red Emission Center at 640 nm

The emission band at 640 nm in forsterite can be assigned to an impurity center of divalent Mn ions as an activator. According to Marfunin (1979) and Götze et al. (1999), the wavelength of this emission clearly depends on the crystal field, which is affected by the ligand oxygens coordinated to the host Mn ion. However, CL spectral data obtained from the Kaba forsterite indicate insufficient information on the coordination effect of an Mn ion in the olivine structure, due to difficulty of discrimination in wavelength between M1 and M2 sites, which could be occupied by Mn ions. On the other hand, Mn can be very low in refractory forsterite; concentrations of only 25 μg g^{-1} have been analyzed by Pack et al. (2005).

In Allende and Murchison forsterite, a broad, but weak, peak occurs near 640 nm, whereas at low temperature, this peak remains broad (Benstock et al. 1997). Benstock et al. (1997) concluded that this peak is assigned to Mn almost certainly in octahedral coordination and probably concentrated in the M2 site (McCormick et al. 1987), compared with synthetic Mn-doped forsterite (Steele 1988). In principle, the emission should differ between Mn sited on M1 and M2, and the position and shape of the emission peaks may reflect site occupancy factors. Taftø and Spence (1982), McCormick et al. (1987), and Buseck and Self (1992) have used atom location by channeling-enhanced microanalysis to determine site occupancy of minor elements in olivine. Mn strongly partitioned into M2 suggests that the variation of CL peak position and shape may not be sensitive enough to record occupancy variations (Benstock et al. 1997), because M2 sites have a lower crystal field associated with the broadening of an emission peak than M1.

Red Emission Centers between 700 and 800 nm

Cathodoluminescence emissions at around 700–800 nm in the red region have been attributed to Mn^{2+} in the M2 site and to Cr^{3+} in the M1 and/or M2 sites (Green and Walker 1985; Steele and Smith 1986; Benstock et al. 1997). The presence of Cr^{2+} in the refractory forsterite grains may also be considered as

they formed under highly reducing conditions (as also indicated by the presence of Tr^{3+}).

The red CL emission centers are present at identical wavelengths in Allende, Murchison, as well as Cr^{3+}-doped synthetic forsterite samples (Benstock et al. 1997), but are not present in the pure synthetic forsterite. Moncorgé et al. (1991) studied synthetic Cr^{3+}-doped forsterite in a cooled sample using fluorescence spectroscopy and found broad emission centers at around 700 nm indicating the temperature dependence of this emission peak. Wood et al. (1968) and Sviridov et al. (1973) identified Cr^{3+}-related (with octahedral coordination) red CL peaks in spinel, ruby, garnets, and emerald. The broad peak near 700 nm at room temperature and the series of sharp peaks at low temperature result from Cr^{3+} in octahedral coordination, either the M1 or M2 site, or both, in the forsterite structure (Benstock et al. 1997). The 800 nm emissions both at room temperature and at low temperature were observed in the spectra of meteoritic and synthetic forsterite samples, which were assigned to Cr^{3+}, but associated with charge vacancies (Moncorgé et al. 1991).

Hydrothermal Alteration of Kaba Meteorite

Relationship between CL and Chemical Variation

The chemical zoning in forsterite grains within chondrite was reported in detail by Jones and Carey (2006). They categorized four zoning patterns as follows: Type CLA (homogeneous), Type CLB (slightly varying), Type CLC (oscillatory), and Type CLD (heterogeneous). Based on this classification criterion, the results obtained here indicate that grains from the B-1 and B-4 areas correspond to type CLB and those from the B-2 area to type CLC.

According to previous studies, forsterite with CL zoning was observed in carbonaceous, ordinary, unequilibrated, and R chondrites. Pack and Palme (2003) and Pack et al. (2004) described the relationship between the CL image and distribution of minor elements in Fe-poor forsterite in Allende, Vigarano, Dar al Gani 013, and Chainpur. Steele (1995) observed that the Cr content of forsterite shows a gradual change with CL intensity, but he noted that there is no qualitative correlation between the CL intensity and the concentrations of other elements, such as Al, Ti, V, and Sc. The CL intensity of experimentally grown forsterite resembling the luminescent meteoritic forsterite increases with an increase in Ca, Al, and Ti contents (Pack and Palme 2003). According to Jones and Carey (2006), Mg-rich forsterite grains (>Fo_{98}) in FeO-poor chondrules in the Mokoia meteorite show variations in CL intensity, which are related to variations in Al_2O_3 and TiO_2 concentrations. Luminescent forsterites in the Kaba meteorite exhibit a feature that their CL intensity decreases toward the outer edge of the grain with decreasing Ca, Al, and Ti concentrations. This fact is not concordant with the results reported by Steele (1995) and Jones and Carey (2006), but conforms to the conclusion by Pack and Palme (2003). Some previous studies on forsterites with CL zoning (e.g., Steele et al. 1985; Klerner et al. 2000) discussed the origin of refractory forsterite, and its formation mechanism as either condensate from early solar nebula or a melt-grown crystal.

Estimation of Temperature of the Alteration Process

In this study, the discussion of the origin of CL zoning recorded on forsterite has emphasized diffusion of the elements by high-temperature metamorphism and hydrothermal metasomatic reaction caused by aqueous alteration. Cation diffusion in olivine was extensively examined by Spandler and O'Neill (2009), suggesting that most of the trace elements diffuse through olivine at similar rates as the major octahedral cations of Fe and Mg. In the case of the Kaba meteorite, moderate thermal metamorphism could be expected to have affected the chondrules possibly at metamorphic temperature below 300 °C. Therefore, Al diffusion (Spandler and O'Neill 2009) from the rim of the olivine across the grain boundary seems to be less likely than accepting elevated temperature up to 300 °C without any hydrothermal reaction.

Oxidized CV3 chondrites of the Bali type (Bali, Kaba, portions of Mokoia, Grosnaja, and ALH 85006) have experienced significant secondary processing (Krot et al. 1995, 1998). In the Kaba meteorite, alteration of chondrule mesostasis (Keller and Buseck 1990) and associated redistribution of Ca, Si, Al, Mg, Fe, Mn, and Na (Krot et al. 1998) are best understood in terms of aqueous alteration on the parent body. Other features in the Kaba meteorite, including Fe-rich halos around some opaque nodules and veins of fayalitic olivine within forsterite grains, are more likely due to high-temperature processing (e.g., Hua et al. 2005). A metasomatic reaction could explain the movement of diffusible ions Ca, Al, and Ti. The migration of these elements can result from simultaneous elimination of intrinsic structural defects progressively from the rim of the grain to the core in the Kaba forsterite. Kayama et al. (2010) investigated the peak changes (i.e., disappearance) of a blue emission peak at 420 nm in alkali feldspar and they found that the elimination of $Al\text{-}O^{-}\text{-}Al$ defect center was affected by hydrothermal metasomatism possibly at 250 °C. This defect center has been often found in plagioclase. The plagioclase in the mesostasis embedded in the Kaba chondrule gives a

weak board emission peak in blue CL region recorded from the outer part of the grain. This indicates that the Kaba feldspar was affected by hydrothermal reactions, which occurred at <250 °C and in a reducing environment different from terrestrial conditions associated with iddingsite. Hence, we can deduce that the Kaba forsterite reacted with a hydrothermal solution, which may have leached out movable elements such as Fe from the rim of the forsterite, resulting in a relative enrichment of refractory minor elements such as Ca and Al in the core. In this case, the survival core of the host forsterite would be observed in the blue CL region, but the red luminescence would correspond to the rim with the elimination of the defect center during hydrothermal process. The Al-O^--Al defect center is eliminated by hydrothermal metasomatism beneath the sanidine-microcline transition temperature (approximately 450 °C) (Finch and Klein 1999), which is in a good agreement with CL data on forsterite observed in this study.

Petrov et al. (1989) reported an ESR signal assigned to Al-O-Al defect center in albite, which disappears by annealing at 250 °C. This temperature is also concordant with that in the case of alkali feldspar suggested by Finch and Klein (1999) and Kayama et al. (2010). Our study also confirms that the Al-O-Al defect is related to the blue emission, which is eliminated by heating at 250 °C not only in alkali feldspar but also in plagioclase.

Formation of the Zoned Olivine

Two scenarios are proposed for formation of zoned olivine in the Kaba meteorite based on the results obtained in this study. (1) The olivine grain originally was formed during melt and condensation processes in the early solar system. (2) The migration due to thermal metasomatism and aqueous alteration on asteroids was responsible for the crystallization process.

Pack et al. (2004) suggested that the refractory (RF) materials crystallized from melts are primary condensates from an interstellar gas. The continuous change in melt composition is then recorded in the decreasing Ca and Al contents of the crystallizing forsterite.

We suggest that metasomatic reactions are important considerations for element migration in minerals and promote the migration of diffusible ions Ca, Al, and Ti in the forsterite structure, which simultaneously causes an elimination of intrinsic structural defects progressively from the rim of the grain to the core. A hydrothermal process could have played a key role in the explanation of the blue CL emission corresponding to not only unaltered survival of the core of the host forsterite, but could also explain the red luminescence from the rim by the elimination of the defect center.

It is important to note that the driving force of diffusion of Fe, Mn, and Cr is still not well understood. The possible explanation could be the incorporation of Fe, Mn, and Cr from a hydrothermal fluid into olivine accompanied by leaching out of Al, Ca, and Ti.

Forsterite from the Kaba Meteorite: Implications for Astromineralogy

Protoplanetary and planetary nebula as postasymptotic giant branch objects are enriched in dust substance in forms of disks, or inhomogeneous clouds. Exact chemical-mineralogical composition of this dust substance is the subject of comprehensive analysis. In the spectra of protoplanetary and planetary nebula are detected narrow faint emissions with unknown nature. We considered these unidentified emissions as a main clue for determination of composition of the circumstellar dust. In different galactic objects, dusty substance might be organic or silicate. The latter case is the subject of our interest. Combination of optical methods of laboratory astrophysics with high-resolution astrospectroscopy is conditioned determination of chemical-mineralogical composition of the cosmic dust. Photoluminescence and cathodoluminescence of forsterite micrograins might be detected in protoplanetary and planetary nebula. Forsterite micrograins might be the component of O-rich planetary nebula dust. Several O-rich objects are candidates for comprehensive investigations, for example, NGC 2392 and NGC3242. Forsterite minerals from Kaba meteorite and other samples might be investigated with the following strategy: (1) cooling of forsterite micrograins to temperature below 80K; (2) enrichment of forsterite micrograins with additional ions by means of ion implantation methods; (3) exciting of photoluminescence and cathodoluminescence of enriched forsterite micrograins; registration of luminescence spectra; (4) direct comparison of laboratory luminescence spectra of forsterite micrograins with optical spectra of astrophysical objects (nebula, comets). In general, analysis of the luminescence spectra peculiarities of forsterite micrograins in wide astrophysical context may provide us with additional data on formation and evolution of silicate minerals in the galaxy and in the solar system particularly. At low temperature, we can detect narrow and faint luminescence emissions of forsterite as components of nebula and comet dust (Simonia and Mikailov 2006; Simonia 2007, 2011). Potential future studies might comprise also the following directions: (1) spectroscopic investigations of blue excess of planetary nebula; (2) photometric investigations of blue reflection nebula illuminated by late spectral type

stars. The 420–550 nm part of forsterite luminescence spectra must be used in mentioned investigations as comparative or analogous laboratory data. Taking into account interests of astromineralogy it will be reasonable to create an atlas of luminescence spectra of forsterite micrograins and other silicate minerals from Kaba and other meteorites. Such a database might become an effective tool for determination of chemical-mineralogical composition of cosmic dust.

Finally, it is important to emphasize that there are various carrier candidates of blue luminescence of interstellar and circumstellar dust as well as molecules that have been discussed extensively in the previous studies. Particularly, potential polycyclic aromatic hydrocarbon luminescence in the form of complex molecules was proposed in the work of Vijh et al. (2004, and references therein). They found that the properties of this luminescence are related to the specific factors, such as quantum yield, spectral position, and profile. In the case of blue luminescence by forsterite grains spectral position, profile, and quantum yield of this nonthermal emission will be noticeably different.

CONCLUSIONS

Our systematic SEM–CL and EMPA studies on forsterite grains in the Kaba meteorite typically show well-ordered crystalline domains with defects more frequent at the grain rims and less typical in the grain cores, which may result from hydrothermal alteration at 250 °C.

We conclude that the apparently high-T nebular features (e.g., low-Fe forsterite, chondrule glass, etc.) can be attributed to low-T parent body processing.

Acknowledgments—AG was partly supported by Max Planck Society (Germany, 2007–2009) and JSPS Long-term Visiting Professorship (Japan) in 2011/12. Authors express thanks to Profs Sumit Chakraborty, Andreas Pack, and Shogo Tachibana for their useful comments on this paper. Authors are grateful to Mr. Richard William McIntosh (Department of Mineralogy and Geology, University of Debrecen) for checking English of this manuscript. KM was supported by TÁMOP 4.2.2/B-10/1-2010-0024 project.

Editorial Handling—Dr. Gopalan Srinivasan

REFERENCES

Benstock E. J., Buseck P. R., and Steele I. M. 1997. Cathodoluminescence of meteoritic and synthetic forsterite at 296 and 77 K using TEM. *American Mineralogist* 82:310–315.

Bonal L., Quirico E., Bourot-Denise M., and Montagnac G. 2006. Determination of the petrologic type of CV3 chondrites by Raman spectroscopy of included organic matter. *Geochimica and Cosmochimica Acta* 70:1849–1863.

Buseck P. R. and Self P. 1992. Electron energy loss spectroscopy (EELS) and electron channeling (ALCHEMI). *Mineralogical Society of America Reviews in Mineralogy* 27:141–180.

Choi B.-G., Krot A. N., and Wasson J. T. 2000. Oxygen isotopes in magnetite and fayalite in CV chondrites Kaba and Mokoia. *Meteoritics & Planetary Science* 33:1065–1085.

Finch A. A. and Klein J. 1999. The causes and petrological significance of cathodoluminescence emissions from alkali feldspar. *Contributions to Mineralogy and Petrology* 135:234–243.

Götze J., Plötze M., Fuchs H., and Habermann D. 1999. Defect structure and luminescence behaviour of agate—Results of electron paramagnetic resonance (EPR) and cathodoluminescence (CL) studies. *Mineralogical Magazine* 63:149–163.

Green G. R. and Walker G. 1985. Luminescence excitation spectra of Mn^{2+} in synthetic forsterite. *Minerals Physics and Chemistry of Minerals* 12:271–278.

Gucsik A., Endo T., Nakazato E., Nishido H., Ninagawa K., Kayama M., Bérczi S., Nagy S., Ábrahám P., Kimura Y., Gyollai I., Simonia I., Rózsa P., Posta J., Nagy M., Mihályi K., Apai D., and Futó P. 2011. Cathodoluminescence characterization of the forsterite in Kaba meteorite: An astromineralogical application (abstract #1157). 42nd Lunar and Planetary Science Conference. CD-ROM.

Gucsik A., Tsukamoto T., Kimura Y., Miura H., Nishido H., Kayama M., Ninagawa K., and Endo T. 2012. Cathodoluminescence microcharacterization of the experimentally grown of forsterite chondrule produced under super cooling. *Journal of Luminescence* 132:1041–1047.

Hezel D. C. and Kießwetter R. 2010. Quantifying the error of 2D bulk chondrule analyses using a computer model to simulate chondrules (SIMCHON). *Meteoritics & Planetary Science* 45:555–571.

Hezel D. C., Russell S. S., Ross A. J., and Kearsley A. T. 2008. Modal abundances of CAIs: Implications for bulk chondrite element abundances and fractionations. *Meteoritics & Planetary Science* 43:1879–1894.

Hua X. and Buseck P. R. 1995. Fayalite in the Kaba and Mokoia carbonaceous chondrites. *Geochimica et Cosmochimica Acta* 59:563–578.

Hua X. and Buseck P. R. 1998. Fayalitic halos around inclusions in forsterites from carbonaceous chondrites. *Geochimica et Cosmochimica Acta* 62:1443–1458.

Hua X., Huss G. R., Tachibana S., and Sharp T. G. 2005. Oxygen, silicon, and Mn-Cr isotopes of fayalite in the Kaba oxidized CV3 chondrite: Constraints for its formation history. *Geochimica et Cosmochimica Acta* 69:1333–1348.

Jones R. H. and Carey E. R. 2006. Identification of relict forsterite grains in forsterite-rich chondrules from the Mokoia CV3 carbonaceous chondrite. *American Mineralogist* 91:1664–1674.

Kayama M., Nakano S., and Nishido H. 2010. Characteristics of emission centers in alkali feldspar: A new approach by using cathodoluminescence spectral deconvolution. *American Mineralogist* 95:1783–1795.

Keller L. P. and Buseck P. R. 1990. Aqueous alteration in the Kaba CV3 carbonaceous chondrite. *Geochimica et Cosmochimica Acta* 54:2113–2120.

Klerner S., Jones R. H., Palme H., and Shearer C. K. 2000. Trace elements and cathodoluminescence in refractory forsterite from Allende and Kaba (abstract #1689). 31st Lunar and Planetary Science Conference. CD-ROM.

Kornacki A. S. and Wood J. A. 1984. The mineral chemistry and origin of inclusion matrix and meteorite matrix in the Allende CV3 chondrite. *Geochimica et Cosmochimica Acta* 48:1663–1676.

Krot A. N., Scott E. R. D., and Zolensky M. E. 1995. Mineralogical and chemical modification of components in CV3 chondrites: Nebular or asteroidal processing? *Meteoritics* 30:748–775.

Krot A. N., Petaev M. I., Scott E. R. D., Choi B., Zolensky M. E., and Keil K. 1998. Progressive alteration in CV3 chondrites: More evidence for asteroidal alteration. *Meteoritics & Planetary Science* 33:1065–1085.

Marfunin A. S. 1979. *Spectroscopy, luminescence and radiation centers in minerals*. Berlin: Springer.

McCormick T. C., Smyth J. R., and Lofgren G. E. 1987. Site occupancies of minor elements in synthetic olivines as determined by channeling enhanced X-ray emission. *Minerals Physics and Chemistry of Minerals* 14:368–372.

Moncorgé R., Cormier G., Simkin D. J., and Capobianco J. A. 1991. Fluorescence analysis of chromium-doped forsterite (Mg_2SiO_4). *Journal of Quantum Electronics* 27:114–120.

Nishido H., Endo T., Ninagawa K., Kayama M., and Gucsik A. 2013. Thermal effects on cathodoluminescence in forsterite. *Geochronometria* 40:239–243. doi:10.2478/s13386-013-0116-7.

Pack A., and Palme H. 2003. Partitioning of Ca and Al between forsterite and silicate melt in dynamic systems with implications for the origin of Ca, Al-rich forsterites in primitive meteorites. *Meteoritics & Planetary Science* 38:1263–1281.

Pack A., Yurimoto H., and Palme H. 2004. Petrographic and oxygen-isotopic study of refractory forsterites from R-chondrite Dar al Gani 013 (R3.5–6), unequilibrated ordinary and carbonaceous chondrites. *Geochimica et Cosmochimica Acta* 68:1135–1157.

Pack A., Palme H., and Shelley J. M. G. 2005. Origin of chondritic forsterite grains. *Geochimica et Cosmochimica Acta* 69:3159–3182.

Petrov I., Agel A., and Hafner S. S. 1989. Distinct defect centers at oxygen positions in albite. *American Mineralogist* 74:1130–1141.

Simon B. S., Sutton R. S., and Grossman L. 2008. Constraints on the oxidation state of chondrule precursors from titanium XANES analysis of Semarkona chondrules (abstract #1352). 39th Lunar and Planetary Science Conference. CD-ROM.

Simonia I. A. 2007. Luminescence of cosmic dust—A result of the interaction of radiation with solid matter. *Astrophysics* 50:548–560.

Simonia I. A. 2011. Organic component of cometary ice. *Astrophysics and Space Science* 332:91–98.

Simonia I. A. and Mikailov K. M. 2006. Photoluminescence and cathodoluminescence by cosmic dust. *Astronomy Reports* 50:960–964.

Slaby E., Götze J., Simon K., and Wörner G. 2008. K-feldsper phenocrysts in microgranular magmatic enclaves: Cathodoluminescence and geochemical studies on crystal growth as a marker of magma mingling dynamics. *Lithos* 105:8597.

Spandler C. and O'Neill H. St. C. 2009. Diffusion and partition coefficients of minor and trace elements in San Carlos olivine at 1300 °C with some geochemical implications. *Contributions to Mineralogy and Petrology* 159:791–818.

Steele I. M. 1988. *Primitive material surviving in chondrites — Mineral grains, Meteorites and the early solar system (A89–27476 10–91)*. Tucson, Arizona: University of Arizona Press. pp. 808–818.

Steele I. M. 1995. Oscillatory zoning in meteoritic forsterite. *American Mineralogist* 80:823–832.

Steele I. M. and Smith J. V. 1986. Contrasting forsterite compositions for C2, C3, and UOC meteorites; evidence for divergence from common parent (abstract). 17th Lunar and Planetary Science Conference. p. 822.

Steele I. M., Smith J. V., and Sirikus C. 1985. Cathodoluminescence zoning and minor elements in forsterites from the Murchison (C2) and Allende (C3V) carbonaceous chondrites. *Nature* 313:294–297.

Stevens-Kalceff M. A. 2009. Cathodoluminescence microcharacterization of point defects in α-quartz. *Mineralogical Magazine* 73:585–605.

Sviridov D. T., Sevastyanov B. K., Orekhova V. P., and Sviridova R. K. 1973. Optical absorption spectra of excited Cr31 ions in magnesium spinel at room and liquid nitrogen temperatures. *Optics and Spectroscopy* 35:59–61.

Taftø J. and Spence J. C. H. 1982. Crystal site location of iron and trace elements in a magnesium-iron olivine by a new crystallographic technique. *Science* 218:49–51.

Valera M. E., Metrich N., Bonnin-Mosbah M., and Kurat G. 2000. Carbon in glass inclusions of Allende, Vigarano, Bali and Kaba (CV3) olivines. *Geochimica et Cosmochimica Acta* 64:3923–3930.

Vijh U. P., Witt A. N., and Gordon K. D. 2004. Discovery of blue luminescence in the red rectangle: possible fluorescence from neutral polycyclic aromatic hydrocarbon molecules? *The Astrophysical Journal* 606:L65–L68.

Wood D. L., Imbusch G. F., MacFarlane R. M., Kisliuk P., and Larkin D. M. 1968. Optical spectrum of Cr31 ions in spinels. *Journal of Chemical Physics* 48:5255–5263.

SUPPORTING INFORMATION

Additional supporting information may be found in the online version of this article:

Fig. S1: X-ray maps of Mg, Fe, Ca, Mn, Al, Cr, Ni, and Ti in the rounded olivine grain of the Kaba meteorite. Ca and Al concentrate in the core of the grain and are almost undetectable in the rim, but the variations of the other concentrations cannot be well evaluated because of low intensities of their signals. The matrix enclosing the olivine grain consists mainly of Ca-Al-rich region.

Fig. S2: X-ray mapping of Mg, Fe, Ca, Mn, Al, Cr, Ni, and Ti in the porphyritic olivine grains in chondrule (B-2 area) reveals that the olivine grain is surrounded by mesostasis phases consisting of Ca-Al-rich material and has a Ca-Al-rich region in the core, consistent with CL image. The concentrations of Ca and Al seem to increase slightly toward the rim from the center of the grain.

Fig. S3: X-ray mapping of Mg, Fe, Ca, Mn, Al, Cr, Ni, and Ti indicates lower amounts of Ca and Al in the rim than those in core of the coarse olivine grain embedded in matrix (B-4 area).